IET Control Theory & Applications

The Institution of Engineering and Technology WILEY

ORIGINAL RESEARCH

Adaptive sliding-mode-assisted disturbance observer-based decoupling control for inertially stabilized platforms with a spherical mechanism

Dapeng Tian[1,2] | **Meiyu Wang**[1,2] | **Fuchao Wang**[1] | **Rui Xu**[1]

[1]Key laboratory of Airborne Optical Imaging and Measurement, Changchun Institute of Optics, Fine Mechanics and Physics, Chinese Academy of Sciences, Changchun, People's Republic of China

[2]University of Chinese Academy of Sciences, Beijing, People's Republic of China

Correspondence

Fuchao Wang and Rui Xu, Key laboratory of Airborne Optical Imaging and Measurement, Changchun Institute of Optics, Fine Mechanics and Physics, Chinese Academy of Sciences, Changchun 130033, People's Republic of China.
Email: fuchaow@163.com; xur@ciomp.ac.cn

Abstract

An inertially stabilized platform (ISP) is a gimbal used to hold a camera. It is essential for isolating the attitude sway during an imaging process. To make the platform more compact, the implementation of an ISP with a spherical mechanism has been proposed. However, this design introduces complex non-linear coupling characteristics, significantly increasing the complexity of control. This study aims to solve this problem and present an algorithm to achieve high-performance inertial stabilization control. To achieve this, kinematic and dynamic models were established, and the proposed control algorithm was then designed in three parts. Gravity compensation control was set up in the internal loop to counter the influence of unbalanced gravity moment. An adaptive sliding-mode-assisted disturbance observer (ASMADO) was also included in the joint space to decouple the influence of complex non-linear characteristics on the platform. Further, a feedback controller was added to the workspace based on the kinematic model. This design simplifies the control algorithm for novel ISPs with a spherical mechanism. It effectively compensates for the complex non-linear characteristics and enables superior inertial stabilization control. Experimental results show that the proposed method effectively decreases the motion isolation error for the line-of-sight of the camera compared to traditional control methods.

1 | INTRODUCTION

An inertial stabilization platform (ISP) is a mechanism installed on a moving carrier to isolate the attitude disturbance of the carrier by controlling the rotation of the platform and the three respective axes. The platform-installed load maintains a stable attitude in the inertial space. An ISP is an essential device used to isolate the attitude motion of a vehicle [1, 2]. Camera-carrying ISPs are widely used in aerial remote sensing and vehicle-mounted or shipborne optical monitoring to obtain clear and stable images [3–5]. ISPs are generally motor-driven multi-axis mechanical frames. In traditional designs, the axes are generally perpendicular to each other [6]. As a result, the motors and corresponding sensor are symmetrically arranged around the central cameras, which limits the camera mounting space. Therefore, to carry a larger caliber camera, mechanical frames are often larger in size, which increases the weight and size of the system. Thus, the installation space of the camera is limited within a fixed size and weight range [7].

A tandem spherical mechanism with three degrees of freedom is a potential solution to this problem. By making the axes intersect at acute angles, the motors and corresponding sensors can be placed centrally. More open installation space can be reserved for the camera. However, in a traditional ISP, the original roll, pitch, and yaw motion of the camera are driven by their respective motors. If a spherical mechanism is employed to build an ISP, each attitude motion would be driven by multiple motors. Additionally, owing to the central installation of the motors, mechanical balancing is challenging. More complex coupled kinematics and dynamics are introduced in the ISP. Further, as in traditional ISP, friction and other non-linear disturbance torques still exist in each axis [8]. These factors

significantly increase the difficulty of inertial stabilization control for such an ISP.

To achieve superior control performance, the coupled motion and dynamics must be compensated. The primary task is to handle complex disturbances. In previous works, several researchers proposed inertial stabilization control algorithms that simplify the ISP into several independent motor driven frames. To weaken the influence of non-linear disturbances in the system, several non-linear control methods have been proposed [9–11].

Robust control methods are highly stable and reliable [12], but they generally require a high-order controller that is impractical to engineer. Sliding mode controls are insensitive to changes in system parameters and disturbances [13]. However, there is a "chattering phenomenon", which becomes more significant with the increase of switching gain. The neural network-based control method is computationally complex and is not suitable for application in ISPs with real-time requirements [14, 15]. Additionally, double-compensated controllers [16] or active disturbance suppression control based on the least mean multiplication method [17] have also been used to compensate disturbances caused by changes in parameters. These simplified treatments have largely facilitated the design of the controller. In the traditional ISP control method, the kinematics and dynamics are simple and decoupled. However, controlling an ISP with the coupled characteristics of a spherical mechanism remains a problem. Further, even in an effectively designed gimbal system, dynamic mass imbalances always exist, degrading the control performance. Therefore, uncertain dynamics need to be considered [18–20].

An ISP with a spherical mechanism is a special control system. Each degree of freedom of the camera's line-of-sight is coupled with the motion of more than two motors. Traditional simplification is not feasible in this case. Coupling is a common problem in multi-degree-of-freedom parallel actuators, such as Delta mechanisms and Stewart platforms [21]. For such parallel mechanisms, model-free control strategies [22] or neural network methods [23] have been used to handle the uncertainty and coupled motion. However, these algorithms are limited by large-scale real-time computational problems. Therefore, to solve the problem of redundancy in the control algorithm [24, 25], made improvements to the common Stewart platform by proposing a decoupling mechanism. However, not every parallel mechanism can achieve simplified control through effective design.

Further, compared with a parallel mechanism, the ISP with a spherical mechanism has a certain particularity [26]. This type of actuator has three rotational degrees of freedom that differ from parallel Delta and Stewart platforms. The three attitude motions, namely, roll, pitch, and yaw, are driven by three rotational motors. There are no complex multiple-motion pairs, such as the use of spherical, revolute, and planar pairs simultaneously in a single actuator. Therefore, a systematized controller design for the ISP with a spherical mechanism is necessary but has not been developed.

The present study aims to fill this gap in ISP development. Considering the disadvantages of traditional frame structure photoelectric stabilization platforms, such as large volume, heavy weight, and small load ratio, this study adopts the photoelectric stabilization platform scheme with a compact spherical mechanism. Although the motors of the spherical mechanism are concentrated together to expand the load installation space, there is still no complete solution to the unbalanced mechanical structure problem and the kinematic-dynamic coupling. In this study, the kinematics and dynamics model of the spherical mechanism is established first, and an unbalanced torque compensation controller is designed based on the model. For the kinematic coupling problem between the workspace and the joint space, a Jacobian matrix is derived to establish the mapping relationship between them. Aiming at solving the coupling problem in dynamics, an adaptive sliding-mode-assisted disturbance observer (ASMADO) is used to observe and compensate the coupling term. Compared with the traditional DOB, the inner loop controller enhances the ability of the system to suppress complex disturbances, which is the main objective of decoupling design . It is worth noting that the application of the ASMADO on the photoelectric stabilization platform of the spherical mechanism is an extension of this method, which enables the application of this type of controller in the complex multi-input and -output system. Furthermore, a feedback controller is designed in the outer loop (workspace) to track the three-axis attitude velocity command. Thus, the controller follows a complete and systematic strategy.

The remainder of this paper is organized as follows. Section 2 establishes the kinematic and dynamic models of the ISP with a spherical mechanism and presents the control problem. Section 3 describes the control strategy design. In Section 4, the proposed control method is verified via experimental results. Finally, Section 5 summarizes the study.

2 | MODELING AND PROBLEM FORMULATION

In this study, an ISP with series spherical mechanism was used to achieve camera movement in the roll, pitch, and yaw dimensions. The angles of all the links of the platform can be determined by a set of 3×1 joint vectors. The space formed by these joint vectors is the joint space. The set of spatial points accessible to the reference points describing the motion of the load camera is the workspace. To realize the control of the ISP, a set of oriented series spherical mechanism coordinate systems was first established. Then, the control problem was formulated.

2.1 | Coordinate system

The spherical mechanism consists of three rotating pairs and three rods connecting the movable base and the camera load at the end of the mechanism. The three axes of the three rotating pairs intersect at one point in the inertial space. The three axes are distributed on the three sides of the tetrahedron, and the angle between any two axes is acute. However, the angles of the photoelectric stabilization platform of the traditional frame
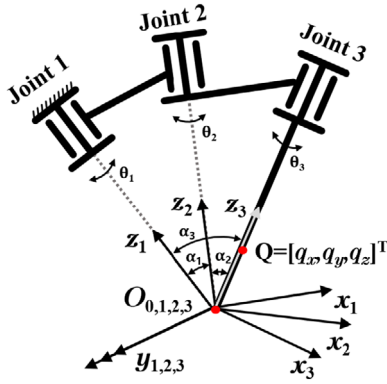
FIGURE 1 Coordinate system for ISP with spherical mechanism

TABLE 1 D-H parameter table

i-1	*i*	*i*+1	θ_{i-1}	α_i
0	1	2	θ_0	α_1
1	2	3	θ_1	α_2
2	3	–	θ_2	α_3

structure are all right angles, so the proposed spherical mechanism design scheme provides a larger load installation space. Figure 1 shows a schematic of the coordinate system that illustrates the relationship between the joints and linkage angles of the mechanism. Unlike the orthogonal frames, this mechanism has a compact structure in which the rotating pairs intersect obliquely. The three axes of rotation intersect in space at a point O. The rotating pairs 1, 2, and 3 move on a spherical surface with O as the center. Let the center of the sphere be the origin of the coordinate system.

$\{O\}$ is the global coordinate system in the inertial space; $\{O_0\}$ is the local coordinate system connecting to the base of the ISP, which coincides with the global coordinate system. $\{O_{1,2,3}\}$ are the local coordinates of the joints 1, 2, and 3, respectively. α_i indicates the relative angle between the z_{i-1} axis and the z_i axis, that is, the angle between the joint axes. θ_{i+1} indicates the angle between the x_i axis and the x_{i+1} axis, that is, the rotation angle of the joint.

In Figure 1, Q is a point on the camera mounted on the ISP with a spherical mechanism. A vector is used to represent the position of the point Q in space. The position vector of Q in the coordinate system $\{O_0\}$ is $[q_x, q_y, q_z]^T$. The position vector of Q in the coordinate system $\{O_3\}$ is $[0, 0, 1]^T$, where q_x, q_y, and q_z are the camera's roll, pitch, and yaw angles, respectively.

The D-H parameters of the spherical mechanism (shown in Table 1) can be used for modeling. The direction of the rotating pair of the series spherical mechanism was selected as the z-direction of the coordinate system, the common perpendicular direction of the plane where the mechanism link and the rotating pair axis are located was selected as the x-direction, and the y-direction was determined by the right-hand rule. Accordingly,

the coordinate system of the series spherical mechanism was established, as shown in Figure 1.

According to the coordinate transformation principle of the D-H method, the transformation matrix $\mathbf{T}_i^{i+1}$ from coordinate system $\{O_i\}$ to coordinate system $\{O_{i+1}\}$ is as follows

$$\mathbf{T}_0^1 = \begin{bmatrix} \cos\theta_0 & -\sin\theta_0 & 0 \\ \cos\alpha_1\sin\theta_0 & \cos\theta_0\cos\alpha_1 & -\sin\alpha_1 \\ \sin\theta_0\sin\alpha_1 & \cos\theta_0\sin\alpha_1 & \cos\alpha_1 \end{bmatrix}, \quad (1)$$

$$\mathbf{T}_1^2 = \begin{bmatrix} \cos\theta_1 & -\sin\theta_1 & 0 \\ \cos\alpha_2\sin\theta_1 & \cos\theta_1\cos\alpha_2 & -\sin\alpha_2 \\ \sin\theta_1\sin\alpha_2 & \cos\theta_1\sin\alpha_2 & \cos\alpha_2 \end{bmatrix}, \quad (2)$$

$$\mathbf{T}_2^3 = \begin{bmatrix} \cos\theta_2 & -\sin\theta_2 & 0 \\ \cos\alpha_3\sin\theta_2 & \cos\theta_2\cos\alpha_3 & -\sin\alpha_3 \\ \sin\theta_2\sin\alpha_3 & \cos\theta_2\sin\alpha_3 & \cos\alpha_3 \end{bmatrix}. \quad (3)$$

2.2 | Kinematic modeling

To describe the kinematics conversion process clearly, the derivation is performed by considering the point Q on the series spherical mechanism as an example. Suppose that the position vector of Q in the global coordinate system $\{O_0\}$ is $[q_x, q_y, q_z]^T$. The position vector of Q in the coordinate system $\{O_3\}$ is $[0, 0, 1]^T$. Then, the relationship between the global coordinate system and the local coordinate system of the mechanism is as follows

$$Q = \begin{bmatrix} q_x & q_y & q_z \end{bmatrix}^T = \mathbf{T}_0^3 \begin{bmatrix} 0 & 0 & 1 \end{bmatrix}^T, \quad (4)$$

$$\mathbf{T}_0^3 = \mathbf{T}_0^1 \mathbf{T}_1^2 \mathbf{T}_2^3 = \begin{bmatrix} t_{11} & t_{12} & t_{13} \\ t_{21} & t_{22} & t_{23} \\ t_{31} & t_{32} & t_{33} \end{bmatrix}. \quad (5)$$

Positive kinematics is the process of solving for the attitude of the load camera based on the angle of each joint. Suppose that the rotation angles are $[\theta_0, \theta_1, \theta_2]^T$ of the rotating sub in the joint space and the transformation matrix $\mathbf{T}_0^3$. Then, the attitude angles $[q_x, q_y, q_z]^T$ in the workspace can be expressed as

$$\begin{cases} q_x = A\tan 2\left(t_{32}/\cos q_y, t_{33}/\cos q_y\right) \\ q_y = A\tan 2\left(-t_{31}^2, \sqrt{t_{11}^2 + t_{21}^2}\right) \\ q_z = A\tan 2\left(t_{21}/\cos q_y, t_{11}/\cos q_y\right). \end{cases} \quad (6)$$

Suppose that the desired attitude angles are $[q_x, q_y, q_z]^T$. Solving for them yields the joint rotation angle θ_i.

$$\begin{cases} \theta_0 = \arctan\left(q_7, \pm\sqrt{q_8^2 - q_7^2}\right) - \arctan(q_9, q_{10}) \\ \theta_1 = \arccos\dfrac{\cos\alpha_2\cos\alpha_3 - (q_1\cos\alpha_2 - q_2\sin\alpha_2)}{\sin\alpha_2\sin\alpha_3}, \\ \theta_2 = \arctan\left(q_3, \pm\sqrt{q_4^2 - q_3^2}\right) - \arctan(q_5, q_6) \end{cases} \quad (7)$$

where

$$\begin{aligned} q_1 &= \cos q_y \cos q_z \\ q_2 &= -\sin q_z \cos q_x + \sin q_x \sin q_y \cos q_z \\ q_3 &= -\sin q_y \cos q_z - \sin q_x \cos q_y \sin q_z \\ q_4 &= \sqrt{q_5^2 + q_6^2} \\ q_5 &= \sin\theta_1 \sin\alpha_2 \\ q_6 &= \cos\theta_1 \sin\alpha_2 \cos\alpha_3 + \sin\alpha_3 \cos\alpha_2 \\ q_7 &= \cos\theta_1 \cos\theta_2 - \sin\theta_1 \cos\alpha_3 \sin\theta_2 \\ q_8 &= \sqrt{q_9^2 + q_{10}^2} \\ q_9 &= \cos q_x \cos q_y \\ q_{10} &= \sin q_x \cos q_y \cos q_z - \sin q_y \sin q_z. \end{aligned} \quad (8)$$

The mapping of the position relationship between joint space and workspace has been established above. To obtain the velocity mapping relationship, the angle vector is derived, which gives following Jacobi matrix:

$$\mathbf{J} = \begin{bmatrix} J_{11} & J_{12} & J_{13} \\ J_{21} & J_{22} & J_{23} \\ J_{31} & J_{32} & J_{33} \end{bmatrix}, \quad (9)$$

where

$J_{11} = \sin\theta_1 \sin\alpha_1$

$J_{12} = \cos\theta_2 \sin\theta_1 \sin\alpha_1 + \cos\alpha_1 \sin\theta_1 \sin\alpha_2$
$\qquad + \cos\theta_1 \cos\alpha_2 \sin\theta_2 \sin\alpha_1$

$J_{13} = \cos\alpha_1(\cos\theta_3 \sin\theta_2 \sin\alpha_2 + \cos\alpha_2 \sin\theta_3 \sin\alpha_3$
$\qquad + \cos\theta_2 \cos\alpha_3 \sin\theta_3 \sin\alpha_3)$
$\qquad + \sin\theta_1 \sin\alpha_1(\cos\theta_2 \cos\theta_3 - \cos\alpha_3 \sin\theta_2 \sin\theta_3)$

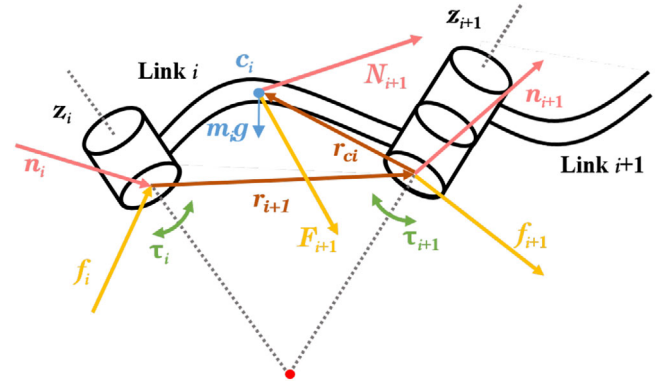**FIGURE 2** Force analysis of an ISP with a spherical mechanism

$\qquad + \cos\theta_1 \sin\alpha_1(\cos\theta_3 \cos\alpha_2 \sin\theta_2 - \sin\theta_3 \sin\alpha_2 \sin\alpha_3$
$\qquad + \cos\theta_2 \cos\alpha_2 \cos\alpha_3 \sin\theta_3)$

$J_{21} = \cos\theta_1 \sin\alpha_1$

$J_{22} = \cos\theta_2 \cos\alpha_1 \sin\theta_2 - \sin\theta_1 \sin\theta_2 \sin\alpha_1$
$\qquad + \cos\theta_1 \cos\theta_2 \cos\alpha_2 \sin\alpha_1$

$J_{23} = \cos\alpha_1(\cos\theta_3 \cos\alpha_2 \sin\alpha_3 - \sin\theta_2 \sin\theta_3 \sin\alpha_2$
$\qquad + \cos\theta_2 \cos\theta_3 \cos\alpha_3 \sin\alpha_2)$
$\qquad - \sin\theta_1 \sin\alpha_1(\cos\theta_2 \sin\theta_3 + \cos\theta_3 \cos\alpha_3 \sin\theta_2)$
$\qquad - \cos\theta_1 \sin\alpha_1(\cos\alpha_2 \sin\theta_2 \sin\theta_3 + \cos\theta_3 \sin\alpha_2 \sin\alpha_3$
$\qquad - \cos\theta_2 \cos\theta_3 \cos\alpha_2 \cos\alpha_3)$

$J_{31} = \cos\alpha_1$

$J_{32} = \cos\alpha_1 \cos\alpha_2 - \cos\theta_1 \sin\alpha_1 \sin\alpha_3$

$J_{33} = \cos\alpha_1(\cos\alpha_2 \cos\alpha_3 - \cos\theta_2 \sin\alpha_2 \sin\alpha_3)$
$\qquad - \cos\theta_1 \sin\alpha_1(\cos\alpha_3 \sin\alpha_2 + \cos\theta_2 \cos\alpha_2 \sin\alpha_3)$
$\qquad + \sin\theta_1 \sin\theta_2 \sin\alpha_1 \sin\alpha_3 \quad (10)$

2.3 | Dynamic modeling

Figure 2 shows the force on the mechanism. In the figure, c_i is the center of mass of the joint i_{th}. $m_i g$ is the gravitational force of the joint i_{th}. $\mathbf{F}_i \in R^3$, $N_i \in R$, respectively, are the inertial force and inertial torque acting on the center of mass of the connecting rod in the coordinate system $\{O_i\}$. $\mathbf{f}_i \in R^3$, $n_i \in R$, respectively, are the inertial force and inertia torque acting on joint i_{th} in the coordinate system $\{O_i\}$ from joint $(i-1)_{th}$. $\mathbf{r}_{i+1} \in R^3$ is the vector of distances from joint i_{th} to joint $(i+1)_{th}$. $\mathbf{r}_{ci} \in R^3$ is the vector of distances from joint i_{th} to the center of mass of the connecting rod i_{th}. $\tau_i \in R^3$ is the torque on joint i_{th}. $\mathbf{n}_i \in R^3$, $\mathbf{f}_i \in R^3$, respectively, represent the inertial forces and moments of inertia of joint $(i-1)_{th}$ on joint i_{th} in the coordinate system $\{O_i\}$.

Combining the Newton-Euler recurrence dynamics equations, the inertial torque on the connecting rod i_{th} is calculated as (11).

$$\mathbf{n}_i = \mathbf{N}_i + \mathbf{T}_{i+1}^i \mathbf{n}_{i+1} + \mathbf{r}_{c_i} \times \mathbf{F}_i + \mathbf{v}_{i+1} \times \mathbf{T}_{i+1}^i \mathbf{f}_{i+1}. \qquad (11)$$

The joint torque is then calculated based on the component of the torque applied by link i_{th} to link $(i + 1)_{th}$ in the z direction.

$$\boldsymbol{\tau} = \begin{bmatrix} \tau_1 \\ \tau_2 \\ \tau_3 \end{bmatrix} = \begin{bmatrix} \mathbf{n}_1^T \mathbf{Z}_1 \\ \mathbf{n}_2^T \mathbf{Z}_2 \\ \mathbf{n}_3^T \mathbf{Z}_3 \end{bmatrix}, \qquad (12)$$

where $\mathbf{Z}_i = [0 \quad 0 \quad 1]^T$ denotes the unit vector of the coordinate system $\{O_i\}$ in the z direction. The detailed solution procedure can be found in Appendix A.

Considering the existence of unmodeled forces in the system, such as friction and external disturbances on the frames, they are uniformly recorded as forces $\mathbf{F}(\boldsymbol{\Theta})$.

Let $\boldsymbol{\Theta} = [\theta_1, \theta_2, \theta_3]^T$, $\boldsymbol{\Theta}, \dot{\boldsymbol{\Theta}}, \ddot{\boldsymbol{\Theta}} \in R^3$ represent the angle vector, angular velocity vector, and angular acceleration vector, respectively, of the connecting rods. The dynamical equation can be written as (13).

$$\mathbf{M}_l(\boldsymbol{\Theta})\ddot{\boldsymbol{\Theta}} + \mathbf{C}_l(\boldsymbol{\Theta}, \dot{\boldsymbol{\Theta}})\dot{\boldsymbol{\Theta}} + \mathbf{G}(\boldsymbol{\Theta}) + \mathbf{F}(\boldsymbol{\Theta}) = \boldsymbol{\tau}. \qquad (13)$$

$\mathbf{M}_l(\boldsymbol{\Theta})$ is the inertia matrix of the mechanism. $\mathbf{C}_l(\boldsymbol{\Theta}, \dot{\boldsymbol{\Theta}})$ is the Coriolis and centrifugal force matrix of the mechanism. $\mathbf{G}(\boldsymbol{\Theta})$ represents the gravity terms.

$$\mathbf{M}_l(\boldsymbol{\Theta}) = \begin{bmatrix} M_{11} & M_{12} & M_{13} \\ M_{21} & M_{22} & M_{23} \\ M_{31} & M_{32} & M_{33} \end{bmatrix}, \qquad (14)$$

$$\mathbf{C}_l(\boldsymbol{\Theta}, \dot{\boldsymbol{\Theta}}) = \begin{bmatrix} C_{11} & C_{12} & C_{13} \\ C_{21} & C_{22} & C_{23} \\ C_{31} & C_{32} & C_{33} \end{bmatrix}, \qquad (15)$$

$$\mathbf{G}(\boldsymbol{\Theta}) = \begin{bmatrix} G_1 \\ G_2 \\ G_3 \end{bmatrix}, \qquad (16)$$

$G_1 = a_3 m_3 g(\sin\theta_3 \cos\alpha_1 \sin\alpha_2 \sin\theta_1$

$\qquad + \cos\alpha_2 \cos\theta_2 \sin\alpha_1 \sin\theta_1 + \cos\theta_3 \sin\alpha_1 \sin\theta_1 \sin\theta_2),$

$\qquad - a_2 m_2 g \sin\alpha_1 \sin\theta_1 \sin\theta_2$

$\qquad\qquad\qquad\qquad\qquad\qquad\qquad\qquad (17)$

$G_2 = - a_3 m_3 g \sin\theta_3 (\cos\alpha_2 \sin\alpha_1 \sin\theta_1$

$\qquad + \cos\theta_1 \sin\alpha_2 \sin\theta_2 + \cos\alpha_1 \cos\theta_2 \sin\alpha_2 \sin\theta_1),$

$\qquad\qquad\qquad\qquad\qquad\qquad\qquad\qquad (18)$

$$G_3 = 0. \qquad (19)$$

Here, m_i is the mass of the rod. Gravitational acceleration $k_g = [0 \quad 0 \quad -g]^T = [0 \quad 0 \quad -9.8]^T$. a_i is the length of the connecting rod i_{th}.

The ISP is a coupled mechanism. The rotation of the connecting rod i_{th} affects that of the connecting rod $(i + 1)_{th}$. This complexity negatively affects the design of the controller. In this study, the system is decoupled based on the principle of treating non-linear coupling terms as disturbances.

Suppose that

$$\mathbf{M}_l(\boldsymbol{\Theta}) = \mathbf{M}(\boldsymbol{\Theta}) + \Delta\mathbf{M}(\boldsymbol{\Theta})$$

$$= \begin{bmatrix} M_{11} & 0 & 0 \\ 0 & M_{22} & 0 \\ 0 & 0 & M_{33} \end{bmatrix} + \begin{bmatrix} 0 & M_{12} & M_{13} \\ M_{21} & 0 & M_{23} \\ M_{31} & M_{32} & 0 \end{bmatrix}, \qquad (20)$$

$$\mathbf{C}_l(\boldsymbol{\Theta}, \dot{\boldsymbol{\Theta}}) = \mathbf{C}(\boldsymbol{\Theta}, \dot{\boldsymbol{\Theta}}) + \Delta\mathbf{C}(\boldsymbol{\Theta}, \dot{\boldsymbol{\Theta}})$$

$$= \begin{bmatrix} C_{11} & 0 & 0 \\ 0 & C_{22} & 0 \\ 0 & 0 & C_{33} \end{bmatrix} + \begin{bmatrix} 0 & C_{12} & C_{13} \\ C_{21} & 0 & C_{23} \\ C_{31} & C_{32} & 0 \end{bmatrix}. \qquad (21)$$

The dynamical equation can be rewritten as

$$\begin{cases} \mathbf{M}(\boldsymbol{\Theta})\ddot{\boldsymbol{\Theta}} + \mathbf{C}(\boldsymbol{\Theta}, \dot{\boldsymbol{\Theta}})\dot{\boldsymbol{\Theta}} + \mathbf{G}(\boldsymbol{\Theta}) = \boldsymbol{\tau} + \mathbf{d}(\boldsymbol{\Theta}, \dot{\boldsymbol{\Theta}}, \ddot{\boldsymbol{\Theta}}) \\ \mathbf{d}(\boldsymbol{\Theta}, \dot{\boldsymbol{\Theta}}, \ddot{\boldsymbol{\Theta}}) = \Delta\mathbf{M}(\boldsymbol{\Theta})\ddot{\boldsymbol{\Theta}} + \Delta\mathbf{C}(\boldsymbol{\Theta}, \dot{\boldsymbol{\Theta}})\dot{\boldsymbol{\Theta}} + \mathbf{F}(\boldsymbol{\Theta}), \end{cases} \qquad (22)$$

where $\mathbf{M}(\boldsymbol{\Theta})$ is the equivalent inertia matrix, $\mathbf{C}(\boldsymbol{\Theta}, \dot{\boldsymbol{\Theta}})$ is the equivalent damping ratio, and $\mathbf{d}(\boldsymbol{\Theta}, \dot{\boldsymbol{\Theta}}, \ddot{\boldsymbol{\Theta}})$ represent an equivalent disturbance.

2.4 | Problem formulation

In the previous subsections, we presented the complete kinematics and dynamics modeling of the optoelectronic stabilized platform spherical mechanism. According to (6)–(9), it is known that each degree of freedom corresponding to the load camera at the end of the mechanism is driven by two or more rotating pairs. Accordingly, to control the motion of the load camera, a multi-motor coupling control scheme is required. By contrast, according to the dynamic formulas (20)–(22) of the mechanism, this coupling relationship also exists in its dynamic characteristics, that is, the rotating pair movement direction is not in a one-to-one correspondence with the camera movement direction. Following the derivation of the kinematic and dynamic models above, it can be seen that each rotation of the attitude angle of the camera's line of sight is coupled to the rotation of the three joints. To achieve inertial stabilization of such an ISP, $\boldsymbol{\tau}$ must be designed to isolate the attitude motion of the base, which is mounted on a moving carrier. This control quantity should
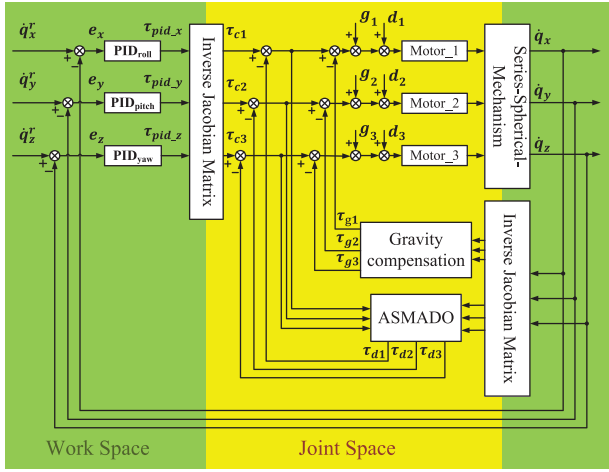
FIGURE 3   Overall control structure of the ISP

handle the gravitational unbalance, coupling, and external disturbances.

3 | PROPOSED CONTROL METHOD

This section presents the controller design for inertial stabilization control of the ISP.

3.1 | Overall control structure

Combined with the general control system, for a complex mechanism with internal and external disturbances, such as an spherical mechanism, relying on a simple DOB alone will be limited by the system bandwidth, resulting in limited system performance. Aiming at the special-controlled object of the spherical mechanism, we propose an ASMADO control method for multi-input and -output systems. The proposed control method not only expands the application scenario of the ASMADO from single-input and -output to multi-input and -output systems, but also realizes the decoupling and high-performance control of the new photoelectric stabilization platform mechanism scheme. The control is composed of three parts. A gravity compensation control $\boldsymbol{\tau}_g$ is designed based on the dynamic model in the joint space. To deal with the coupling and external disturbance, an internal-loop control $\boldsymbol{\tau}_d$ is added based on the concept of an ASMADO. A feedback controller $\boldsymbol{\tau}_c$ is designed to realize the inertial stabilization in the workspace, and a Jacobi matrix is used to connect the workspace and the joint space. The control quantity is designed as

$$\boldsymbol{\tau} = \boldsymbol{\tau}_c - \boldsymbol{\tau}_g - \boldsymbol{\tau}_d. \tag{23}$$

Figure 3 shows the block diagram of the control system. In the workspace, the referred angular velocity vector is $(\dot{q}_x^r, \dot{q}_y^r, \dot{q}_z^r)^T$. The actual angular velocity vector is $(\dot{q}_x, \dot{q}_y, \dot{q}_z)^T$. The error between the expected angular velocity of the camera

and the actual angular velocity response is

$$\mathbf{e}_W = \left[e_{W\dot{x}}, e_{W\dot{y}}, e_{W\dot{z}} \right]^T. \tag{24}$$

In the joint space, the expected angular velocity of the ISP is denoted as $(\dot{\theta}_1^r, \dot{\theta}_2^r, \dot{\theta}_3^r)^T$. The actual angular velocity is $(\dot{\theta}_1, \dot{\theta}_2, \dot{\theta}_3)^T$.

$$\begin{bmatrix} \dot{\theta}_1 \\ \dot{\theta}_2 \\ \dot{\theta}_3 \end{bmatrix} = J^{-1} \begin{bmatrix} \dot{q}_x \\ \dot{q}_y \\ \dot{q}_z \end{bmatrix}. \tag{25}$$

Then, the angular velocity error in the joint space is

$$\mathbf{e}_J = \left[e_{J1}, e_{J2}, e_{J3} \right]^T. \tag{26}$$

The diagram shows the control implementation method in such an ISP.

3.2 | Gravity compensation control

The ISP is an asymmetric structure. The unbalanced moment of gravity affects the inertial stabilization control. Gravity compensation is essential. In this study, active compensation was used to eliminate the influence of unbalanced moments. Let the plane $O_0 - x_0 y_0$ of the global coordinate system $\{O_0\}$ in Figure 1 be the zero point of potential energy. The item of gravity can be compensated by designing the control $\boldsymbol{\tau}_g = [\tau_{g1}, \tau_{g2}, \tau_{g3}]^T$.

$$\begin{cases} \tau_{g1} = G_1 \\ \tau_{g2} = G_2 \\ \tau_{g3} = G_3. \end{cases} \tag{27}$$

3.3 | Design of ASMADO

The function of $\boldsymbol{\tau}_d$ is to suppress non-linear coupling factors and uncertainty perturbations in the system. There is a reasonable assumption.

Assumption 1. [27]: The elements in vector $\mathbf{d}(\boldsymbol{\Theta}, \dot{\boldsymbol{\Theta}}, \ddot{\boldsymbol{\Theta}})$ are unknown and bounded. There exists a positive number d_{boundi} that satisfies

$$\left| \dot{d}_i(\theta, \dot{\theta}, \ddot{\theta}) \right| \leq d_{boundi}. \tag{28}$$

First, a non-linear disturbance observer(DOB) is designed. Let the estimate of disturbance be $\mathbf{d}(\boldsymbol{\Theta}, \dot{\boldsymbol{\Theta}}, \ddot{\boldsymbol{\Theta}})$. The estimation error of the disturbance is

$$\mathbf{e}_d = \mathbf{d}(\boldsymbol{\Theta}, \dot{\boldsymbol{\Theta}}, \ddot{\boldsymbol{\Theta}}) - \mathbf{d}(\boldsymbol{\Theta}, \dot{\boldsymbol{\Theta}}, \ddot{\boldsymbol{\Theta}}). \tag{29}$$

Introducing auxiliary variables $\boldsymbol{\zeta} = [\zeta_1, \zeta_2, \zeta_3]^T$, the DOB is designed as follows

$$\begin{cases} \dot{\boldsymbol{\zeta}} = -\mathbf{L}\boldsymbol{\zeta} - \mathbf{L}(\boldsymbol{\tau}_c + \boldsymbol{\tau}_g + \mathbf{L}\mathbf{M}(\boldsymbol{\Theta})\dot{\boldsymbol{\Theta}} - \mathbf{C}(\boldsymbol{\Theta}, \dot{\boldsymbol{\Theta}})\dot{\boldsymbol{\Theta}}) \\ \mathbf{\hat{d}}(\boldsymbol{\Theta}, \dot{\boldsymbol{\Theta}}, \ddot{\boldsymbol{\Theta}}) = \boldsymbol{\zeta} + \mathbf{L}\mathbf{M}(\boldsymbol{\Theta})\dot{\boldsymbol{\Theta}}, \end{cases} \quad (30)$$

where $\mathbf{L} = \text{diag}[l_1, l_2, l_3]$ is the observer gain.

There is a transition process in the estimation of disturbance by the DOB. An observation error occurs as the disturbance changes. To handle this error, an adaptive sliding mode technique is used to compensate the residual interference quantity $\mathbf{e}_d$ using an additional $\boldsymbol{\tau}_s$.

Consider an auxiliary system with the same dynamic model as the ISP. Suppose that the error between the velocity responses of the real system and the auxiliary system is $\mathbf{e}_J = [e_{J1}, e_{J2}, e_{J3}]^T$ [28]. An integral sliding mode surface is selected as

$$\mathbf{s} = \boldsymbol{\lambda}\mathbf{e}_J + \int_0^t \mathbf{e}_J \, dt, \quad (31)$$

where $\boldsymbol{\lambda} = \text{diag}[\lambda_1, \dots, \lambda_n], \lambda_i > 0$.

The integral sliding mode surface can avoid the second derivative of the variable in the control rate and enhance the stability of the controller.

The approach rate is designed as

$$\dot{\mathbf{s}} = \boldsymbol{\lambda}\dot{\mathbf{e}}_J + \mathbf{e}_J = \hat{\boldsymbol{\eta}}\,\text{sgn}(\mathbf{s}) + \boldsymbol{\varepsilon}\mathbf{s}. \quad (32)$$

where

$$\hat{\boldsymbol{\eta}} = \text{diag}\left[\hat{\eta}_1 \quad \hat{\eta}_2 \quad \hat{\eta}_3\right], \quad (33)$$

$$\boldsymbol{\varepsilon} = \text{diag}\left[\hat{\varepsilon}_1 \quad \hat{\varepsilon}_2 \quad \hat{\varepsilon}_3\right]. \quad (34)$$

Here, $\varepsilon_i > 0$ and $\eta_i > 0$ are constants. $\hat{\eta}_i$ is the variable switching gain that is used to suppress chattering in the system. The adaptation rate is designed

$$\dot{\hat{\eta}}_i = \frac{\sigma_{1i}}{M_{ii}}|s_i| - \frac{\sigma_{2i}}{M_{ii}}\hat{\eta}_i. \quad (35)$$

Here, σ_{1i} and σ_{2i} are positive numbers.

Then, the design of the ASMADO for the ISP with a spherical mechanism can be obtained as follows

$$\begin{cases} \boldsymbol{\tau}_d = \boldsymbol{\tau}_s + \hat{\mathbf{d}}(\boldsymbol{\Theta}, \dot{\boldsymbol{\Theta}}, \boldsymbol{\Theta}) \\ \boldsymbol{\tau}_s = \mathbf{C}(\boldsymbol{\Theta}, \dot{\boldsymbol{\Theta}})\mathbf{e}_J - \mathbf{M}(\boldsymbol{\Theta})\boldsymbol{\lambda}^{-1}\mathbf{e}_J + \hat{\boldsymbol{\eta}}\,\text{sgn}(\mathbf{s}) + \boldsymbol{\varepsilon}\mathbf{s} \end{cases}. \quad (36)$$

The ASMADO method is stable. $\mathbf{e}_d, \mathbf{s}, \mathbf{e}_J$ are ultimately consistent and bounded. For simplification, the proof is provided in Appendix B.

3.4 | Feedback control design

The angular velocity error in the workspace is $\mathbf{e}_W$. Proportional-integral-derivative (PID) control is used to design the feedback controller. First, the PID controller in the workspace is designed as

$$\boldsymbol{\tau}_{pid} = \mathbf{k}_p \mathbf{e}_W + \mathbf{k}_i \int \mathbf{e}_W \, dt + \mathbf{k}_d \dot{\mathbf{e}}_W. \quad (37)$$

$\mathbf{k}_p = [k_{px}, k_{py}, k_{pz}]^T$, $\mathbf{k}_i = [k_{ix}, k_{iy}, k_{iz}]^T$, $\mathbf{k}_d = [k_{dx}, k_{dy}, k_{dz}]^T$ are the gain vectors of the PID controller.

The control $\boldsymbol{\tau}_{pid}$ is a variable of the workspace. The control quantity $\boldsymbol{\tau}_{pid}$ cannot be used directly for the control of the ISP. Then, the vector transformation of $\boldsymbol{\tau}_{pid}$ is used to obtain the control value in the joint space.

$$\boldsymbol{\tau}_c = \mathbf{J}^{-1}\boldsymbol{\tau}_{pid}. \quad (38)$$

Remark 1. The gravity compensation controller, ASMADO, and PID were designed in this study. Among them, the gravity compensation controller does not need to perform the parameter adjustment process. The parameter adjustment processes of the ASMADO and PID controllers are introduced next. Neither the ASMADO nor PID involves the adjustment of a single parameter. Let us take the ASMADO as an example. The ASMADO involves three sets of parameters, $\boldsymbol{\lambda}$, $\boldsymbol{\sigma}_1$, and $\boldsymbol{\sigma}_2$, which should first adjust the switching gain $\boldsymbol{\lambda}$ to achieve stable mechanism control, then adjust the adaptive gain $\boldsymbol{\sigma}_1$, $\boldsymbol{\sigma}_2$ to improve the controller response speed. At the same time, each set of parameters contains three variables, which, respectively, correspond to the three degrees of freedom of the camera. In the parameter adjustment process, it is recommended to follow the order of azimuth, pitch, and roll. When the switching gain $\boldsymbol{\lambda}$ is too large, the system will oscillate; if it is too small, it will not achieve good stability. The parameter adjustment process of adaptive gain $\boldsymbol{\sigma}_1, \boldsymbol{\sigma}_2$ and the PID $\mathbf{k}_p, \mathbf{k}_i, \mathbf{k}_d$ is similar.

Remark 2. The proposed control method is a systematic design framework for systems under coupled complex perturbations with uncertainties. Modelable disturbances such as gravity can be compensated for based on the dynamics model. The other factors are further compensated via an ASMADO-based controller. For the coupling relationship between the workspace and the joint space, the Jacobian matrix can realize the mutual transformation between them. The above design ideas can be extended to other multi-degree-of-freedom parallel actuators or other robots.

4 | EXPERIMENTS

Comparison experiments were implemented to verify the validity of the proposed method. This section describes the development of the experimental system.
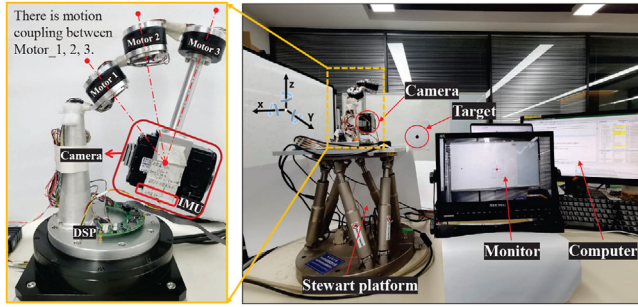
FIGURE 4 Experimental system

4.1 | Experimental setup

Based on the model description in Section 2, a prototype of the photoelectric stabilization platform with a spherical mechanism is established, as shown in Figure 4. It can be clearly seen from the figure that the positional relationship of the three rotating pairs of the experimental prototype is relatively compact, the axes intersect at one point in the inertial space, and any two axes are not orthogonal. To facilitate the experiment, a permanent magnet synchronous motor and an encoder are coaxially installed on the shaft of each joint of the experimental prototype. The encoder can obtain the rotation angle and angular velocity of the motor. The end link is connected to the load frame, and a camera with an image tracking function is installed in the load frame, which can measure the amount of missed target. The monitor can show the real-time tracking image of the camera. An inertial measurement unit (IMU) is installed under the payload frame to measure the real-time pose of the payload camera. The optical axis of the load camera is parallel to the roll axis of the IMU, which is convenient for evaluating the control effect. Above the base of the photoelectric stabilization platform is the experimental prototype controller DSP28335, and the bottom is fixedly connected to the Stewart Platform. When the three roll, azimuth, and pitch directions of the Stewart Platform are given, a sinusoidal command with an amplitude of 7° and a frequency of 300 Hz is applied. Then, the shaking of the Stewart Platform can be regarded as an external disturbance to the prototype. This experiment evaluates the visual axis stability performance of the controller by comparing the ability of the PID, PID+DOB, and the proposed method to isolate the shaking of the Stewart Platform. At the same time, the tracking image and miss amount of the camera can also intuitively reflect the control effect of the controller. Furthermore, to verify the stability and effectiveness of the newly proposed method, the sliding mode surface parameters, adaptive gain parameters, and decoupling effects are also observed and analyzed. The control algorithm design flow is shown in Figure 5.

By removing the internal loop anti-interference control or replacing the ASMADO with a traditional non-linear DOB, comparative cases were also tested to verify the effectiveness of the proposal. Three cases were considered in the experiments: using only PID control, using PID control and the DOB, and using the proposed method.
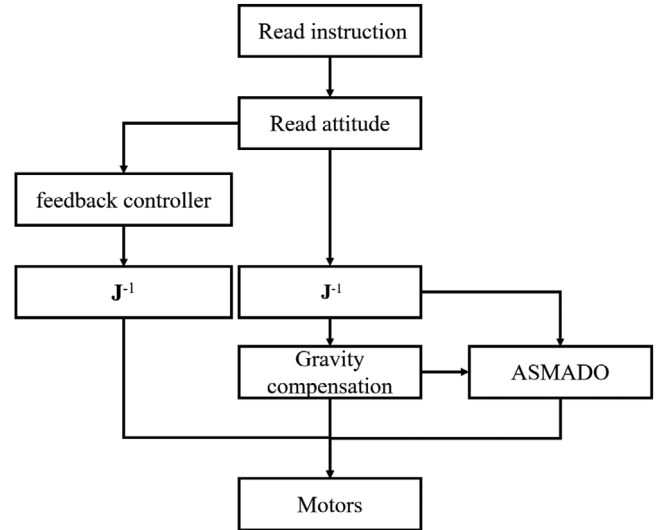

FIGURE 5 Control algorithm design flow

TABLE 2 Experimental parameters

Variable	Motor 1	Motor 2	Motor 3
θ_i	−39.65	26.46	26.46
M	1.42×10^{-4}	6.25×10^{-5}	5.56×10^{-5}
C	0.25×10^{-3}	4.54×10^{-4}	1.67×10^{-4}
K_p	0.006	0.005	0.35×10^{-2}
K_i	0.3	0.2	0.1
λ	0.568	0.137	0.332
ε	0.004	0.53×10^{-2}	0.007
σ_1	0.7	0.6	1.0
σ_2	230	230	200

By identifying the parameters of the experimental ISP in Figure 4, the parameters of the gravity compensation control are

$$\tau_{g_1} = 0.2725 \sin \alpha_1 - 0.0337 \sin \alpha_2 + 0.5237 \sin \theta_1, \quad (39)$$

$$\tau_{g_2} = 0.2383 \sin \alpha_1 + 0.0421 \sin \alpha_2 + 0.1249 \sin \theta_2. \quad (40)$$

Other parameters are given in Table. 2. The sampling time of the control system was 1 ms. To ensure an objective comparison, each control method was given the same gains.

4.2 | Experimental results

Figure 6a–c, respectively, illustrates the attitude of the camera (roll (q_x), pitch (q_y), and yaw ($q_{\bar{z}}$)) under the three control methods. These attitude responses reflect the isolation of the ISP from external movement. Owing to the influence of the unbalanced torque of gravity, the attitude of the mechanism shifts
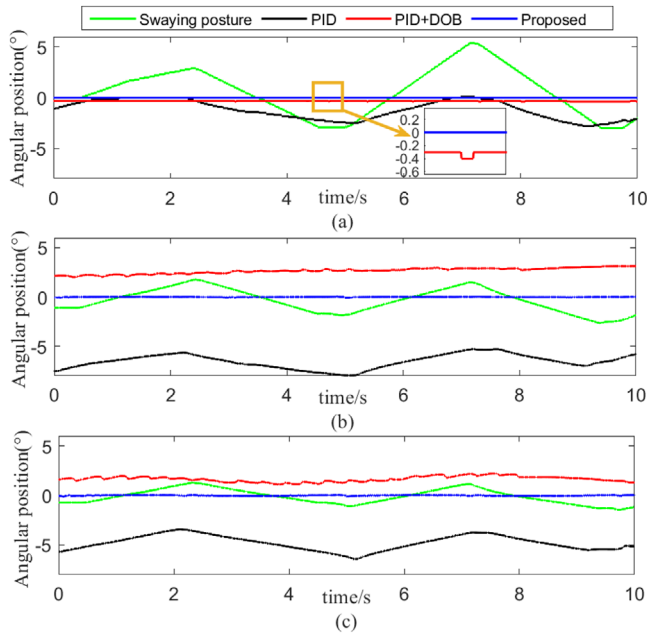
FIGURE 6 Angular position of the IMU in the (a) roll (q_x) direction, (b) pitch (q_y) direction, and (c) yaw (q_z) direction
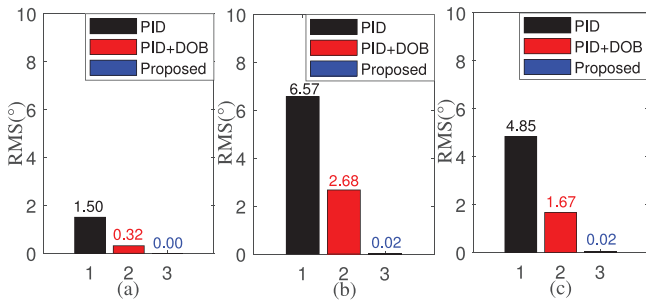

FIGURE 7 RMS values of the angular position. (a) roll direction, (b) pitch direction, (c) yaw direction

FIGURE 8 Angular position of the joint in the (a) roll (q_x), (b) pitch (q_y), and (c) yaw (q_z) directions

FIGURE 9 RMS values of the joint angular position. (a) roll, (b) pitch, and (c) yaw directions

FIGURE 10 Motor control input for the three methods. (a)–(c) joints 1-3, respectively

when only PID or PID with the DOB are used. The attitude does not fluctuate near zero. Figure 7a–c shows the comparison of the root mean square (RMS) error of the attitude responses using the three methods. The proposed method effectively isolates external motion and achieves the smallest error.

Figure 8a–c, respectively, illustrate the attitude of the motor $\theta_1, \theta_2, \theta_3$ under the three control methods. Figure 9a–c show a comparison between the root mean square (RMS) error of the attitude responses using the three methods. The proposed method effectively isolates external motion and achieves the smallest error. The above two sets of curves demonstrate the ability of the controller to interfere with the estimated compensation at each joint.

Figure 10 shows the curve of the control values in each motor. There is no significant oscillation in the control value of the proposed method compared with traditional control methods. The difference between the proposed and traditional methods illustrates the ability to compensate the unbalance torque, coupling, and complex disturbances.
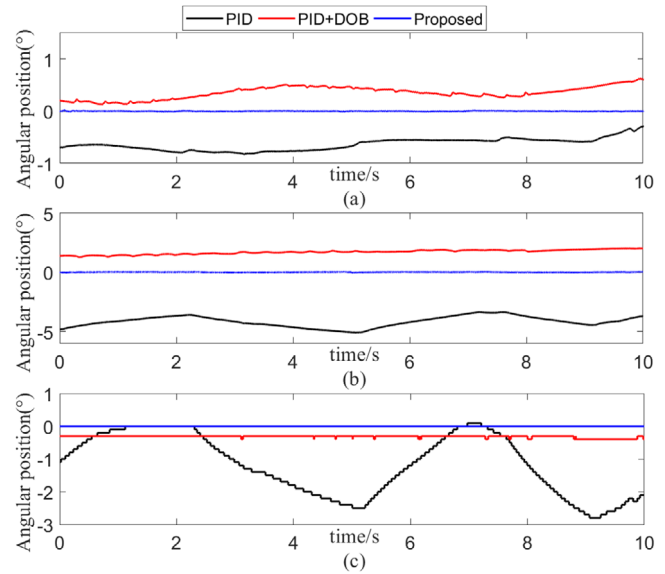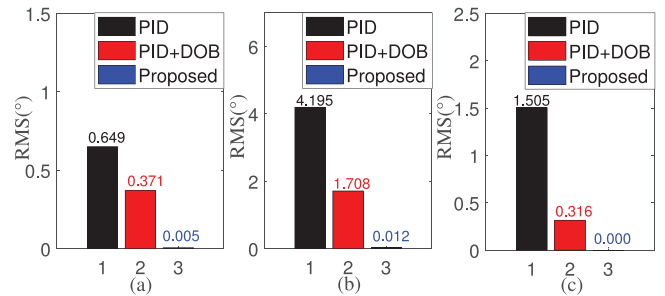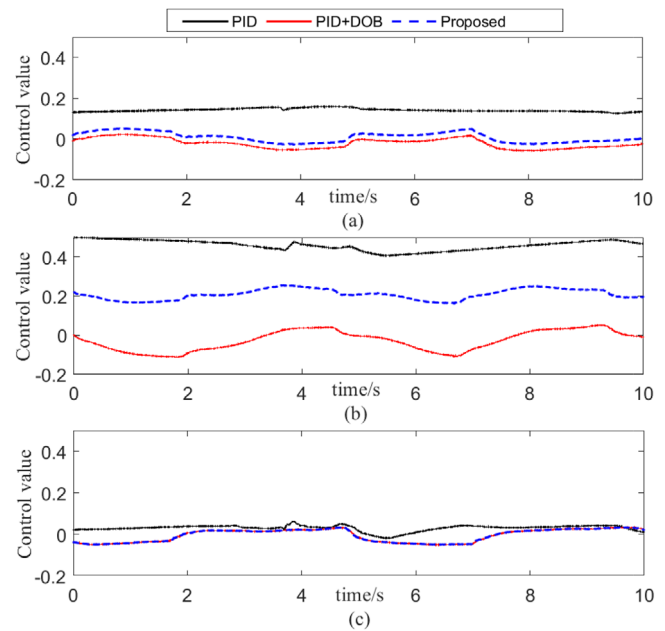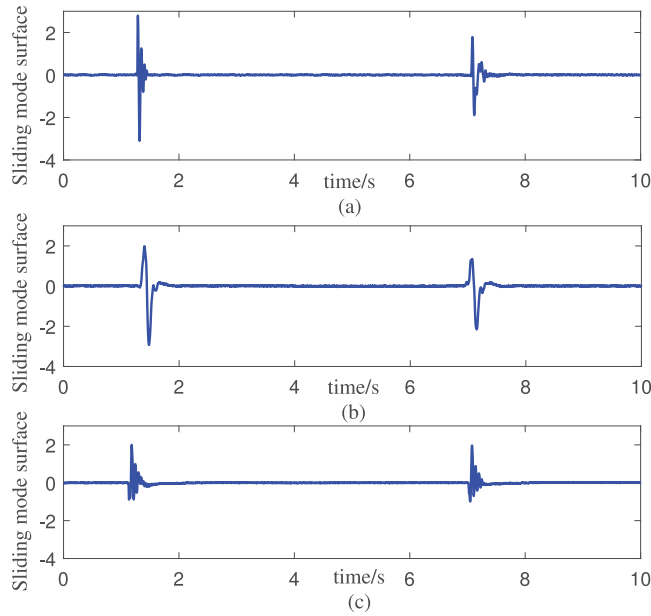
FIGURE 11 Sliding mode surface of ASMADO. (a) joint 1, (b) joint 2, (c) joint 3
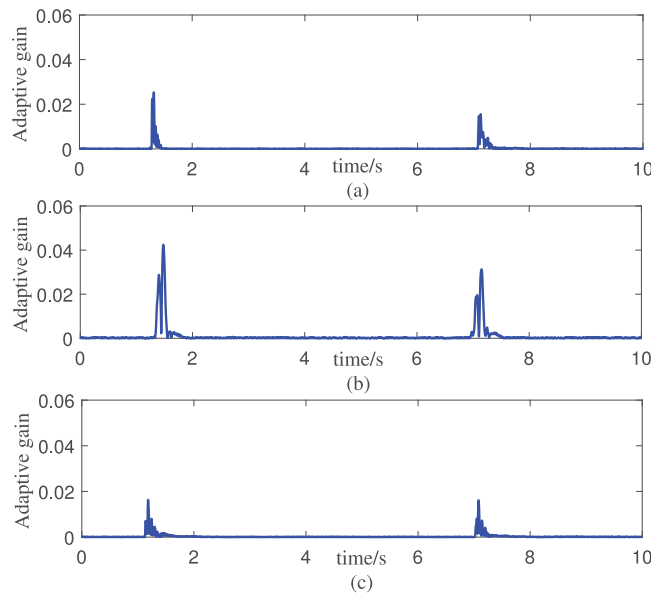

FIGURE 12 Adaptive gain of ASMADO. (a) joint 1, (b) joint 2, (c) joint 3

Figures 11 and 12 capture the curves of the sliding mode surface and adaptive gain of the proposed method, respectively. When the system is subjected to a large external shock, the adaptive gain rapidly increases in response to it. The sliding mode surface rapidly converges toward zero after being subjected to external perturbations. This set of curves demonstrates the existence and convergence of the sliding mode surface of ASMADO.

The mapping of the coupling relationship between the workspace and the joint space in kinematics is established by the Jacobian matrix. In dynamics, the decoupling of the cou-
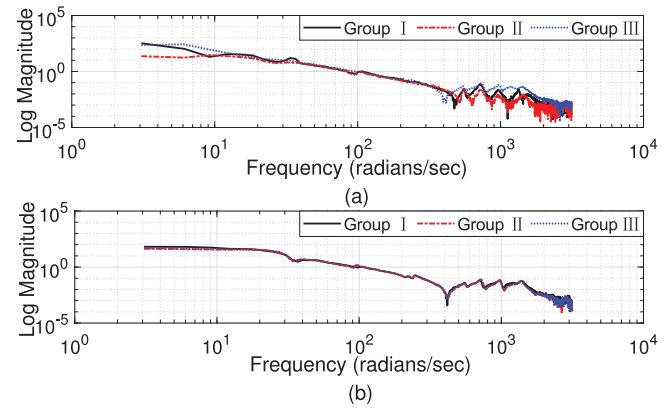

FIGURE 13 Motor 1 model identification results (a) before and (b) after decoupling

pling relationship refers to the separation of $\mathbf{M}$ and $\mathbf{C}$ from $\Delta\mathbf{M}$ and $\Delta\mathbf{C}$, and the coupling separation via the ASMADO. The terms $\Delta\mathbf{M}$ and $\Delta\mathbf{C}$ are estimated and compensated. Thus, the diagonal matrices $\mathbf{C}$ and $\mathbf{C}$ are obtained to realize the decoupling of the system. This can be obtained by observing the difference between the system models with or without ASMADO through the input of a given photoelectric stabilization platform via noise sweeping. The identification results are shown in Figure 13. Figure 13a identifies the system without decoupling, and collects three sets of identification experimental data for motor 1 for comparison. The identification results of each group are different, indicating that motor 1 is affected by the coupling effect of the other two motors at this time. Figure 13b identifies the decoupled system, and also collects three sets of data for motor 1 for comparison with the experimental data without decoupling. The identification results of the three groups after decoupling are basically the same, indicating that motor 1 is not affected by the other motors at this time. Therefore, the proposed method enables the decoupling of the dynamic model.

In the experiments, the inertial stabilization of the three methods is also visually compared with the tracking function of the camera. Figure 14 shows the off-target from the center of the image. Compared to the methods using PID only and PID with the DOB, the proposed method showed optimum isolation from external motion. This is confirmed by the RMS error of the off-target quantities in Figure 15; the off-target quantities are significantly smaller than traditional control methods in both vertical and horizontal directions. Statistically, the proposed method decreases the RMS in vertical and horizontal directions by 36.2% and 46.3%, respectively, compared to the method using PID with the DOB.

In summary, the proposed method has the smallest off-target quantities and the optimum isolation of external motion.

5 | CONCLUSION

The ISP with a spherical mechanism is a gimbal with open installation space for a camera. However, the motion of the
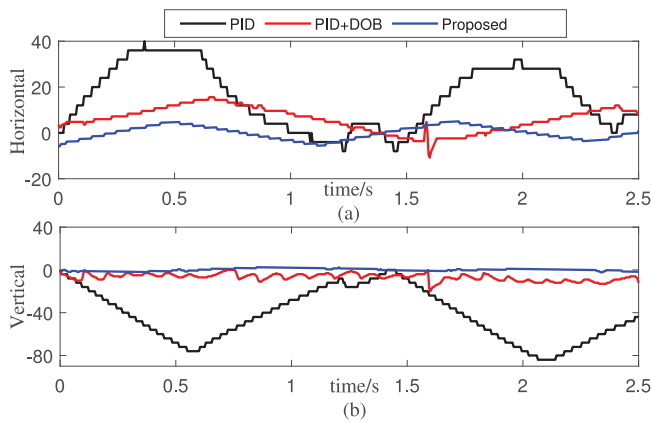
FIGURE 14　Missing quantity comparison chart. (a) Vertical off-target volume and (b) horizontal off-target volume
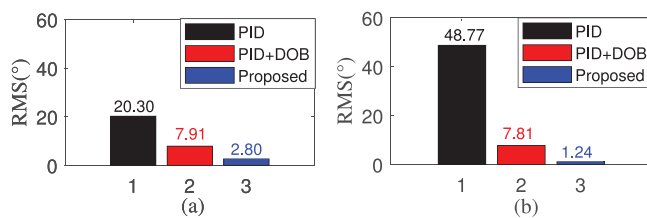

FIGURE 15　Comparative experimental results of off-target quantities. RMS of the (a) vertical off-target volume and (b) horizontal off-target volume

camera in each direction is coupled with the rotation of three joints. In this study, to achieve inertial stabilization control of the coupled system, a kinematic model of the spherical mechanism was established using the D-H parametric method, and a dynamic model was established using the Newton–Euler method. A controller was proposed with three parts. Gravity compensation was designed based on the dynamic model, and an internal loop ASMADO was proposed for the multiple-input multiple-output spherical mechanism. This internal-loop control helps to decouple the control and compensate the complex disturbances. Using a Jacobi matrix, feedback control was also included in the workspace.

The experimental results show that the proposed control method improves the rejection of external interference and reduces the complexity of the system compared with traditional control methods using PID only and PID with a DOB. From both the IMU data and the camera images, it can be concluded that the proposed method solves the problem of stabilization of an ISP with a spherical mechanism.

This paper presents a system design method for an ISP controller with a spherical mechanism. This scheme not only proposes the ASMADO controller for the multi-input and -output system, but also decouples the new mechanism of radio and television stabilization platforms. The proposed scheme has strong engineering application potential. In future work, we intend to design a controller for the attitude angle in the workspace, which can be combined with other functional algorithms to simplify the control algorithm [29, 30] and enhance the control of the coupled spherical mechanism.

CONFLICT OF INTEREST
The authors have declared no conflict of interest.

DATA AVAILABILITY STATEMENT
The data that support the findings of this study are available on request from the corresponding author. The data are not publicly available due to privacy restrictions.

ORCID
Dapeng Tian https://orcid.org/0000-0002-3438-2970
Rui Xu https://orcid.org/0000-0002-8040-2768

REFERENCES
1. Zhao, L., Jia, Y.: Finite-time attitude stabilisation for a class of stochastic spacecraft systems. IET Control Theory Appl. 9(8), 1320–1327 (2015)
2. Sun, S., Zhao, L., Jia, Y.: Finite-time output feedback attitude stabilisation for rigid spacecraft with input constraints. IET Control Theory Appl. 10(14), 1740–1750 (2016)
3. Toth, C., Jóźków, G.: Remote sensing platforms and sensors: A survey. ISPRS J. Photogramm. Remote Sens. 115, 22–36 (2016)
4. Luo, J., Fan, Y., Jiang, P., He, Z., Xu, P., Li, X., et al.: Vehicle platform attitude estimation method based on adaptive kalman filter and sliding window least squares. Meas. Sci. Technol. 32(3), 035007 (2020)
5. Rostovtseva, V., Goncharenko, I., Konovalov, B.: Application of shipborne three-channel hyperspectrometer for remote sensing of coastal marine areas and internal seas. In: OCEANS 2019-Marseille, pp. 1–4. IEEE, Piscataway (2019)
6. Wen, T., Xiang, B.: The airborne inertially stabilized platform suspend by an axial-radial integrated active magnetic actuator system. J. Adv. Res. 31, 191–205 (2021)
7. Safa, A., Yazdanpanah Abdolmalaki, R.: Robust output feedback tracking control for inertially stabilized platforms with matched and unmatched uncertainties. IEEE Trans. Control Syst. Technol. 27(1), 118–131 (2019)
8. Deng, K., Cong, S., Kong, D., Shen, H.: Discrete-time direct model reference adaptive control application in a high-precision inertially stabilized platform. IEEE Trans. Ind. Electron. 66(1), 358–367 (2019)
9. Deng, Y., Wang, J., Li, H., Liu, J., Tian, D.: Speed control of pmsm with sliding mode disturbance observer. In: 2018 IEEE International Conference on Mechatronics and Automation (ICMA), pp. 2311–2315. IEEE, Piscataway (2018)
10. Rubagotti, M., Patrinos, P., Bemporad, A.: Stabilizing linear model predictive control under inexact numerical optimization. IEEE Trans. Autom. Control 59(6), 1660–1666 (2014)
11. Liu, L., Yu, Z., Yu, J., Zhou, Q.: Global output feedback stabilisation for a class of stochastic feedforward non-linear systems with state time delay. IET Control Theory Appl. 9(6), 963–971 (2015)
12. Mao, J., Yang, J., Liu, X., Li, S., Li, Q.: Modeling and robust continuous tsm control for an inertially stabilized platform with couplings. IEEE Trans. Control Syst. Technol. 28(6), 2548–2555 (2020)
13. Dong, F., Lei, X., Chou, W.: A dynamic model and control method for a two-axis inertially stabilized platform. IEEE Trans. Ind. Electron. 64(1), 432–439 (2016)
14. Lei, X., Lu, P.: The adaptive radial basis function neural network for small rotary-wing unmanned aircraft. IEEE Trans. Ind. Electron. 61(9), 4808–4815 (2014)
15. Giap, N.H., Kim, J.H., Kim, H.M., Shin, J.H., Kim, W.H.: Adaptive robust neural network controller for position tracking of ac servo drives. In: 2009

IEEE International Symposium on Industrial Electronics, pp. 1767–1772. IEEE, Piscataway (2009)

16. Deng, J., Xue, W., Zhou, X., Mao, Y.: On disturbance rejection control for inertial stabilization of long-distance laser positioning with movable platform. Meas. Control 53(7-8), 1203–1217 (2020)

17. Bai, C., Zhang, Z.: A least mean square based active disturbance rejection control for an inertially stabilized platform. Optik 174, 609–622 (2018)

18. Sui, S., Zhao, T.: Active disturbance rejection control for optoelectronic stabilized platform based on adaptive fuzzy sliding mode control. ISA Trans. (2021)

19. Battistel, A., Oliveira, T.R.: Unit vector control of an unbalanced three-axis gimbal for application to inertially stabilized platforms. Asian J. Control 23(5), 2157–2170 (2021)

20. He, Q., Zeng, C., Gao, Z., Wu, Z.: Analysis and design of the stewart platform-based parallel support bumper for inertially stabilized platforms. IEEE Trans. Ind. Electron. 67(5), 4203–4215 (2020)

21. Shang, W., Xie, F., Zhang, B., Cong, S., Li, Z.: Adaptive cross-coupled control of cable-driven parallel robots with model uncertainties. IEEE Rob. Autom. Lett. 5(3), 4110–4117 (2020)

22. Boudjedir, C.E., Bouri, M., Boukhetala, D.: Model-free iterative learning control with nonrepetitive trajectories for second-order mimo nonlinear systems-application to a delta robot. IEEE Trans. Ind. Electron. 68(8), 7433–7443 (2021)

23. Nguyen, V.T., Su, S.F., Wang, N., Sun, W.: Adaptive finite-time neural network control for redundant parallel manipulators. Asian J. Control 22(6), 2534–2542 (2020)

24. Ding, B., Cazzolato, B.S., Stanley, R.M., Grainger, S., Costi, J.J.: Stiffness analysis and control of a stewart platform-based manipulator with decoupled sensor-actuator locations for ultrahigh accuracy positioning under large external loads. J. Dyn. Syst. Meas. Contr. 136(6), 061008 (2014)

25. Yang, G., Chen, I.M., Chen, W., Lin, W.: Kinematic design of a six-dof parallel-kinematics machine with decoupled-motion architecture. IEEE Trans. Rob. 20(5), 876–887 (2004)

26. Rosyid, A., El Khasawneh, B., Alazzam, A.: Review article: Performance measures of parallel kinematics manipulators. Mech. Sci. 11(1), 49–73 (2020)

27. Vo, A.T., Kang, H.J.: Adaptive neural integral full-order terminal sliding mode control for an uncertain nonlinear system. IEEE Access 7, 42238–42246 (2019)

28. Liu, J., Li, H., Deng, Y.: Torque ripple minimization of pmsm based on robust ilc via adaptive sliding mode control. IEEE Trans. Power Electron. 33(4), 3655–3671 (2018)

29. Yang, T., Sun, N., Fang, Y.: Adaptive fuzzy control for a class of mimo underactuated systems with plant uncertainties and actuator deadzones: Design and experiments. IEEE Trans. Cybern. 1–14 (2021)

30. Yang, T., Sun, N., Fang, Y.: Neuroadaptive control for complicated underactuated systems with simultaneous output and velocity constraints exerted on both actuated and unactuated states. IEEE Trans. Neural Networks Learn. Syst. 1–11 (2021)

31. Moulay, E., Perruquetti, W.: Finite time stability and stabilization of a class of continuous systems. J. Math. Anal. Appl. 323(2), 1430–1443 (2006)

32. Zhu, Z., Xia, Y., Fu, M.: Attitude stabilization of rigid spacecraft with finite-time convergence. Int. J. Robust Nonlinear Control 21, 686–702 (2011)

APPENDIX A

The derivation of joint torque for a spherical mechanism has two main components. The first extrapolates outwards from link 1 to link 3 to calculate the velocity and acceleration of the links. The second extrapolates from link 3 to link 1 in one iteration, calculating the interaction forces between the links, torque, and driving torque of the joints.

$\boldsymbol{\omega}_i = [0, 0, \omega_i]^T$ is the angular velocity of the joint i_{th}.

$\mathbf{v}_i = [0, 0, v_i]^T$ is the linear velocity of the joint i_{th}.

$\mathbf{v}_{ci} = [0, 0, v_{ci}]^T$ is the linear velocity of the center of mass of the connecting rod i_{th}.

$\mathbf{I}_i \in R^{3 \times 3}$ is the inertia matrix of the connecting rod $i_t h$.

Extrapolation i: $0 \to 2$

$$\boldsymbol{\omega}_{i+1} = \mathbf{T}_i^{i+1}\boldsymbol{\omega}_i + \dot{\theta}_{i+1}\mathbf{Z}_{i+1}, \tag{A.1}$$

$$\dot{\boldsymbol{\omega}}_{i+1} = \mathbf{T}_i^{i+1}\dot{\boldsymbol{\omega}}_i + \mathbf{T}_i^{i+1}\boldsymbol{\omega}_i \times \dot{\theta}_{i+1}\mathbf{Z}_{i+1} + \ddot{\theta}_{i+1}\mathbf{Z}_{i+1}, \tag{A.2}$$

$$\dot{\mathbf{v}}_{i+1} = \mathbf{T}_i^{i+1}\left(\dot{\boldsymbol{\omega}}_i \times \mathbf{r}_{i+1} + \boldsymbol{\omega}_i \times \left(\boldsymbol{\omega}_i \times \mathbf{r}_{i+1}\right) + \dot{\mathbf{v}}_i\right), \tag{A.3}$$

$$\dot{\mathbf{v}}_{c_{i+1}} = \dot{\boldsymbol{\omega}}_{i+1} \times \mathbf{r}_{c_{i+1}} + \boldsymbol{\omega}_{i+1} \times \left(\boldsymbol{\omega}_{i+1} \times \mathbf{r}_{c_{i+1}}\right) + \dot{\mathbf{v}}_{i+1}. \tag{A.4}$$

Summing all the forces acting on the connecting rod i_{th} gives the force balance equation:

$$\mathbf{F}_{i+1} = m_{i+1}\dot{\mathbf{v}}_{c_{i+1}}. \tag{A.5}$$

Torque balance equation:

$$\mathbf{N}_{i+1} = \mathbf{I}_{i+1}\dot{\boldsymbol{\omega}}_{i+1} + \boldsymbol{\omega}_{i+1} \times \mathbf{I}_{i+1}\boldsymbol{\omega}_{i+1}. \tag{A.6}$$

Inward thrust i: $3 \to 1$
Inertial force on connecting rod i_{th}:

$$\mathbf{f}_i = \mathbf{T}_{i+1}^i\mathbf{f}_{i+1} + \mathbf{F}_i. \tag{A.7}$$

Inertial torque on connecting rod i_{th}:

$$\mathbf{n}_i = \mathbf{N}_i + \mathbf{T}_{i+1}^i\mathbf{n}_{i+1} + \mathbf{r}_{c_i} \times \mathbf{F}_i \quad + \mathbf{v}_{i+1} \times \mathbf{T}_{i+1}^i\mathbf{f}_{i+1}. \tag{A.8}$$

The torque of joint i_{th} is

$$\tau_i = \mathbf{n}_i^T\mathbf{Z}_i. \tag{A.9}$$

APPENDIX B

First, three lemmas are given before proving the proposed ASMADO method based on gravity compensation.

Lemma A.1. *[31]: Suppose the first-order non-linear differential inequality is as follows*

$$\dot{V}_1(\theta) \leq -k_{v1}V_1^{\chi_1}(\theta). \tag{B.1}$$

Among them, $V_1(\theta)$ represents the positive Lyapunov function of the state variable $\theta \in R$, $k_{v1} > 0$, $0 < \chi_1 < 1$ positive Lyapunov function.

Then, for any given initial condition $V_1(\theta(0)) = V_1(0)$, the function $V_1(\theta)$ converges to the origin within a given finite time:

$$t_1 \leq \frac{V_1^{1-\chi_1}(0)}{k_{v1}(1-\chi_1)}. \qquad (B.2)$$

Lemma A.2. [32]: Consider a non-linear system $\theta = f(\theta, \mu)$, where θ is the state vector and u is the input vector. Suppose there exists $k_2 > 0$, $0 < \chi_2 < 1$ and $0 < \rho_1 < \infty$, such that the positive definite continuous function $V_2(\theta)$ satisfies

$$\dot{V}_2(\theta) \leq -k_{v2}V_2^{\chi_2}(\theta) + \rho_1. \qquad (B.3)$$

Then, the system can converge in a finite time t_2, where

$$t_2 \leq \frac{V_2^{1-\chi_2}(\theta(0))}{\rho_2 k_{v2}(1-\chi_2)}. \qquad (B.4)$$

In the formula, $0 < \rho_2 < 1$.

Lemma A.3. For $\theta = [\theta_1, \theta_2, \ldots, \theta_n]^T \in R^n$, the following inequality is constant

$$\left(\theta_1^2 + \theta_2^2 + \cdots + \theta_n^2\right)^{\frac{1}{2}} \leq (|\theta_1| + |\theta_2| + \cdots |\theta_n|). \qquad (B.5)$$

The proof of Theorem 1 is given below in three parts.

(1) DOB Stability Proof:

Subject to Equation (30) and Assumption 1 being known, in finite time, the perturbation estimation error e_{di} for the i_{th} motor will converge to

$$\Omega_{1i} = \left\{ e_{di} \| e_{di} | \leq \frac{d_{bound}}{l_i} \right\}. \qquad (B.6)$$

Choose the Lyapunov function:

$$V_d = \frac{1}{2}\mathbf{e}_d^T \mathbf{e}_d. \qquad (B.7)$$

The derivative of the above equation gives

$$\dot{V}_d = \mathbf{e}_d \dot{\mathbf{d}} - \mathbf{L}\mathbf{e}_d^2$$
$$= \sum_{i=1}^{3} e_{di}\dot{d}_i - l_i e_{di}^2$$
$$\leq \sum_{i=1}^{3} d_{boundi}|e_{di}| - l_i e_{di}^2 \qquad (B.8)$$
$$= \sum_{i=1}^{3} -|e_{di}|(l_i|e_{di}| - d_{bound}).$$

If $|e_{di}| \geq d_{boundi}/l_i + k_{v3}$ and $k_{v3} > 0$, Equation (B.8) can be written as

$$\dot{V}_{di} \leq -k_{v3}|e_{di}| = -\sqrt{2}k_{v3}V_{di}^{\frac{1}{2}}. \qquad (B.9)$$

Therefore, according to Lemma A.1, inequality Equation (B.9) can satisfy the stability criterion. At finite time $t_{3i} \leq \frac{\sqrt{2}V_{di}^{\frac{1}{2}}(0)}{\delta\kappa_3}$ with $0 < \delta < 1$, the perturbation estimation error can converge to the bounded set Ω_{1i}.

(2) ASMADO Stability Proof:

Choose the Lyapunov function as follows

$$V_s = \frac{1}{2}\left(\mathbf{e}_d^T \mathbf{e}_d + \mathbf{s}^T \mathbf{s} + \mathbf{e}_\eta^T \boldsymbol{\sigma}_1^{-1} \mathbf{e}_\eta\right). \qquad (B.10)$$

Among them, $\mathbf{e}_\eta = \boldsymbol{\eta} - \hat{\boldsymbol{\eta}}$ and $\eta_i \geq d_i + \gamma_i$ with $\gamma_i > 0$. The derivative of V_s gives

$$\dot{V}_s = \mathbf{e}_d \dot{\mathbf{d}} - \mathbf{L}\mathbf{e}_d^2 + \mathbf{s}^T \dot{\mathbf{s}} - \boldsymbol{\sigma}_1^{-1}\mathbf{e}_\eta \dot{\hat{\boldsymbol{\eta}}}$$

$$= \mathbf{e}_d \dot{\mathbf{d}} - \mathbf{L}\mathbf{e}_d^2 + \mathbf{s}^T(\boldsymbol{\lambda}\dot{\mathbf{e}}_J + \mathbf{e}_J)$$
$$- \sum_{i=1}^{3}\left(\frac{e_{\eta i}}{M_{ii}}|s_i| - \frac{\sigma_{2i}}{M_{ii}\sigma_{1i}}e_{\eta i}\hat{\eta}_i\right)$$

$$= \mathbf{e}_d \dot{\mathbf{d}} - \mathbf{L}\mathbf{e}_d^2 + \mathbf{s}^T[\mathbf{d} - \hat{\mathbf{d}} - \hat{\boldsymbol{\eta}}\,\text{sgn}(\mathbf{s}) - \boldsymbol{\varepsilon}\mathbf{s}]$$
$$- \sum_{i=1}^{3}\left(\frac{e_{\eta i}}{M_{ii}}|s_i| - \frac{\sigma_{2i}}{M_{ii}\sigma_{1i}}e_{\eta i}\hat{\eta}_i\right)$$

$$= \mathbf{e}_d \dot{\mathbf{d}} - \mathbf{L}\mathbf{e}_d^2 + \sum_{1}^{3}s_i\left[d_i - \hat{d}_i - \hat{\eta}_i\,\text{sgn}(s_i) - \varepsilon_i s_i\right]$$
$$- \sum_{i=1}^{3}\left(\frac{e_{Jii}}{M_{ii}}|s_i| - \frac{\sigma_{2i}}{M_{ii}\sigma_{1i}}e_{Jij}\hat{\eta}_i\right)$$

$$\leq \mathbf{e}_d \dot{\mathbf{d}} - \mathbf{L}\mathbf{e}_d^2 + \sum_{1}^{3}\frac{1}{M_{ii}}\left(|d_i - \hat{d}_i||s_i| - \eta_i|s_i| - \varepsilon_i s_i^2\right)$$
$$+ \sum_{i=1}^{3}\frac{\sigma_{2i}}{M_{ii}\sigma_{1i}}e_{Jip}\hat{\eta}_i$$

$$= \mathbf{e}_d \dot{\mathbf{d}} - \mathbf{L}\mathbf{e}_d^2 + \sum_{1}^{3}-\frac{|s_i|}{M_{ii}}\left(\eta_i - |d_i - \hat{d}_i|\right) - \sum_{1}^{3}\frac{\varepsilon_i}{M_{ii}}s_i^2$$
$$+ \sum_{i=1}^{3}\frac{\sigma_{2i}}{M_{ii}\sigma_{1i}}e_{\eta i}\hat{\eta}_i. \qquad (B.11)$$

Known,

$$e_{\eta i}\hat{\eta}_i = e_{\eta i}(\eta_i - e_{\eta i}) \leq \left(\frac{\eta_i^2 - e_{\eta i}^2}{2}\right). \qquad (B.12)$$

After time t_3, (B.11) can be rewritten as follows

$$\dot{V}_s \leq \sum_{i=1}^{3} \left(-k_{v3}|e_{di}| - \frac{\gamma_i}{M_{ii}}|s_i| + \frac{\sigma_{2i}}{J_{ii}\sigma_{1i}}e_{\eta i}\hat{\eta}_i \right)$$

$$\leq \sum_{i=1}^{3} \left(-k_{v3}|e_{di}| - \frac{\gamma_i}{M_{ii}}|s_i| - \frac{\sigma_{2i}|e_{\eta i}|}{2M_{ii}\sigma_{1i}} \right. \qquad \text{(B.13)}$$

$$\left. + \frac{\sigma_{2i}}{2M_{ii}\sigma_{1i}} \left(|e_{\eta i}| + \eta_i^2 - e_{\eta i}^2 \right) \right),$$

where $\gamma_i > 0$. Further, because $\frac{\sigma_{2i}}{2M_{ii}\sigma_{1i}}(|e_{\eta i}| + \eta_i^2 - e_{\eta i}^2)$, there exists upper bound $\omega_i = \frac{\sigma_{2i}+4\sigma_{2i}\eta i^2}{8M_{ii}\sigma_1}$. From Lemma A.3, we can obtain

$$\dot{V}_{si} \leq -\min\left\{ \sqrt{2}k_{v3}, \frac{\sqrt{2}\gamma_i}{M_{ii}}, \frac{\sigma_{2i}}{M_n\sqrt{2\sigma_{1i}}} \right\} \left(\frac{|e_{di}|}{\sqrt{2}} + \frac{|s_i|}{\sqrt{2}} + \frac{|e_{\eta i}|}{\sqrt{2\sigma_{1i}}} \right) + \varphi$$

$$\leq k_{v4}V_{si}^{\frac{1}{2}} + \varphi, \qquad \text{(B.14)}$$

where $k_{v4} = -\min\{\sqrt{2}k_{v3}, \sqrt{2}\gamma_i/M_{ii}, \sigma_{2i}/(M_{ii}\sqrt{2\sigma_{1i}})\}$ Therefore, according to Lemma A.2, the sliding mode surface s_i and $e_{\eta i}$ will converge to approximately zero in a finite time t_{si}, where

$$t_{si} = t_{3i} \frac{\sqrt{2}V_{si}^{\frac{1}{2}}(0)}{\mu k_{v4}}, \quad 0 < \mu < 1. \qquad \text{(B.15)}$$

(3) System Stability Proof:

The Liapunov function is chosen as follows

$$V_e = \frac{1}{2}\mathbf{e}_J^T\mathbf{e}_J. \qquad \text{(B.16)}$$

The derivative of the above equation gives

$$\dot{V}_e = \mathbf{e}_J\dot{\mathbf{e}}_J$$

$$= \frac{1}{\lambda}(\dot{\mathbf{s}} - \mathbf{e}_J)\mathbf{e}_J \qquad \text{(B.17)}$$

$$\leq \sum_{i=1}^{3} \frac{1}{\lambda}\left(\left|e_{Ji}\right| - |s_i|\right)\left|e_{Ji}\right|.$$

If $|e_{Ji}| \geq \lambda|s_i| + k_{v5}$ with $k_{v5} > 0$, Equation (B.17) can be written as follows

$$\dot{V}_{ei} \leq -k_{v5}\left|e_{Ji}\right| = -\sqrt{2}k_{v5}V_{ei}^{\frac{1}{2}}. \qquad \text{(B.18)}$$

Theorem 1 shows that Equation (B.18) can satisfy the convergence criterion. The error e_{Ji} can converge to a bounded set near zero at time $t_{ei} = t_{si} + \sqrt{2}V_{ei}^{\frac{1}{2}}(t_{si})/(\xi k_{v5})$ with $0 < \xi < 1$.

From the above proof, it can be concluded that $\mathbf{s}$, $\boldsymbol{\eta}$, and $\mathbf{e}_J$ are eventually uniformly bounded. Thus, the proposed method is stable.